

Intrinsic permeability of heterogeneous porous media

Wenqiao Jiao

*Institute of Earth Science, University of Lausanne, 1015 Lausanne, Switzerland and
Dipartimento di Ingegneria Civile e Ambientale, Politecnico di Milano, Piazza L. Da Vinci 32, 20133 Milano, Italy*

David Scheidweiler, Nolwenn Delouche, and Pietro de Anna*

Institute of Earth Science, University of Lausanne, 1015 Lausanne, Switzerland

Alberto Guadagnini

*Dipartimento di Ingegneria Civile e Ambientale, Politecnico di Milano, Piazza L. Da Vinci 32, 20133 Milano, Italy and
Department of Hydrology and Atmospheric Sciences, The University of Arizona, Tucson, AZ 85721, USA*

(Dated: June 6, 2024)

Providing a sound appraisal of the nature of the relationship between flow (Q) and pressure drop (ΔP) for porous media is a long-standing fundamental research challenge. A wide variety of environmental, societal and industrial issues, ranging, e.g., from water-soil system remediation to subsurface energy optimization, is affected by this critical issue. While such dependence is well represented by the Kozeny-Carman formulation for homogeneous media, the fundamental nature of such a relationship (Q vs ΔP) within heterogeneous porous systems characterized by a broad range of pore sizes is still not fully understood. We design a set of controlled and complex porous structures and quantify their intrinsic permeability through detailed high quality microfluidics experiments. We synthesize the results upon deriving an original analytical formulation relating the overall intrinsic permeability of the porous structure and their key features. Our formulation explicitly embeds the spatial variability of pore sizes into the medium permeability through a conceptualization of the system as a collection of smaller scale porous media arranged in series. The resulting analytical formulation yields permeability values matching their experimentally-based counterparts without the need of additional tunable parameters. Our study then documents and supports the strong role played by the micro-structure on the overall medium permeability.

INTRODUCTION

Characterization of fluid flow through permeable media is critical in a wide variety of natural and engineered scenarios. These include, for example, riverbank filtration [1], remediation of contaminated soil [2], deep geothermal energy exploration and production [3], nucleation and recurrence of earthquakes [4], and geological CO_2 storage [5]. The structural properties of porous systems that are known to control macroscopic fluid flow, as well as other processes related to mixing of chemicals, include porosity, grain size and shape, tortuosity, effective pore radius, solid surface areas, and pore/grain size distribution [6–11].

In presence of a laminar regime associated with a flow rate Q of a single fluid of dynamic viscosity μ through a porous domain of cross-sectional area A , a continuum (i.e., macroscopic) description of the average fluid velocity q across the system is provided by Darcy’s law [12, 13]

$$q = \frac{Q}{A} = -\frac{k}{\mu} \nabla P. \quad (1)$$

Here, k denotes the intrinsic medium permeability and $\nabla P = \Delta P/L$ is the overall pressure gradient (evaluated along the mean flow direction) induced by a pressure drop ΔP across the domain of size L . The intrinsic permeability k represents the overall ability of the porous system to host a net flow and it is regarded as a key parameter for the porous medium characterization at a continuum (or Darcy) scale [14, 15].

Providing a sound assessment of porous media permeability is still the object of intense research activities. Remarkable efforts have been devoted to explore correlations between permeability and the porous medium internal architecture, as quantified through quantities such as grain and/or pore size distributions, characteristic lengths or porosity [16–24]. Among these studies, the classical Kozeny-Carman formula [25, 26] is broadly employed. Such a formulation is based on a conceptual picture according to which the average (Darcy) velocity through a homogeneous porous medium can be expressed as the corresponding velocity associated with a system composed of a pipes collection with identical diameter (d). Flow within each pipe is, then, expressed through the Hagen-Poiseuille law, which is the exact solution of Stokes equations, representing momentum conservation, for laminar fluid displacement. Within this theoretical formulation, the intrinsic permeability k results to be a function of the medium porosity ϕ , as

$$k = \frac{c_0}{\sigma^2} \frac{\phi^3}{(1-\phi)^2}, \quad (2)$$

where $c_0 = \frac{1}{5}$ is the Kozeny constant and σ denotes the specific surface of the medium grains [25]. The value of σ can be found invoking that the viscous friction experienced by the flowing fluid at the grain walls in the porous medium coincides with its counterpart at the pipe walls. Thus, for a homogeneous porous domain composed by an assemblage of identical spheres, of diameter d_g , $\sigma = \frac{6}{d_g}$, that honors the surface to volume ratio between spheres (the porous medium grains) and pipes (the model). This formatio has been adapted to other homogeneous structures: for instance, considering an assemblage of vertical cylinders as grains, $\sigma = \frac{4}{d_g}$ [21, 27].

A large number of diverse porous systems have an internal structure that is characterized by a complex arrangement of pores. These, in turn, cannot be properly represented through an equivalent spatially homogeneous model of the kind described above and cannot be effectively characterized through a unique (averaged/characteristic) pore/grain size and porosity. Natural porous media are documented to possess a very rich structure in terms of pore and/or throat length distributions (e.g. [28]). For instance, a log-normal function has been found to represent the distribution of pore sizes across glass beads and sand porous materials [29, 30]. Further analyses, performed on clay and sandstone samples through high-resolution imaging technologies (such as BIB-SEM, X-ray μ -CT and FIB-SEM image-stacks) [31] or using small-angle neutron scattering and fluid-invasion methods [32], document power-law pore size distributions, thus highlighting the multi-scale nature of such permeable structures.

Detailed characterizations of complex pore spaces are typically grounded on high-resolution imaging of a given sample, segmentation of the acquired images to identify pores and grains, and ensuing construction of a pore network. The latter step is often performed with methods based on Delaunay Triangulation or Maximum Inscribed Circles (MICs) algorithms [33–36]. While values of average pore size and connectivity have been used to quantify the overall, macroscopic, medium permeability [37], the spatial variability of pore sizes, quantified by their statistical distribution, has been documented to control the local velocity values distribution itself and, hence, asymptotic transport [38]. Moreover, also the spatial correlation of pore sizes has been shown to affect flow and its patterns in porous media [39].

As pore sizes, λ , of natural porous media span across several orders of magnitude, a simplified picture that reduces the complexity of a porous structure to the one of a homogeneous assemblage of identical spheres, is expected to fail in representing heterogeneous systems. Alternative formulations, based on modifications of the Kozeny-Carman formula, propose different relationships between the average pore throat size, effective grain size and medium porosity. Key shortcomings of these models are that these still rely on the use of a single (average/representative) pore throat and/or grain size and that some parameters embedded therein have only minimal (or no) direct connection to the host medium structure and cannot be quantified through direct observations [40, 41].

Advancements in the development of pore network models [42–44] to assess the macroscopic mass transport properties in porous media suggest that the effect of pore connectivity is markedly stronger than the effect of porosity [45]. Moreover, the pore space structure of porous systems can be significantly altered over short time scales by a variety of phenomena such as, e.g., biofilm growth [46], mineral dissolution [47–49] and/or precipitation [50, 51].

For practical reasons, porous samples are typically characterized at scales of a few tens of pores, at best. At this scale, an heterogeneous structure typically result in flow focused in high velocity channels and stagnation zones [38]: a fluid particle entering a fast flow channel will probably never experience low velocities before leaving the medium or, in contrast, can enter the system in a stagnation zone within which it moves very slowly. The description of flow in these scenarios is controlled by the connection between pores, quantified by the system connectivity [52–54]. However, here we consider the scenario of a heterogeneous porous system of size L that is much larger than the average pore size. This scenario virtually corresponds to consider the possibility of scanning a sample across several length-scales (i.e., not just a few tens but several hundreds of average pore sizes). Hence, we hypothesize that each fluid parcel flowing through the porous medium experiences the whole structural variability therein and not only the one of a high velocity channel or a stagnation zone. In other words, we assume that the flow statistics along each trajectory is the same as the ensemble velocity statistics, i.e., the system under consideration is ergodic.

To study such complex media, we design controlled and complex porous structures whose size L is a few hundreds of average pore sizes. These are, then, printed into microfluidics devices that we characterize in terms of their overall permeability k , in presence of laminar flow driven by an imposed macroscopic pressure drop. We show that the ensuing permeability values cannot be interpreted through classical models of the kind described above and based on the use of effective and/or averaged quantities (e.g., representative grain size or porosity). Thus, we derive and test a novel analytical formulation that explicitly embeds the whole range of pore sizes to predict the system permeability. Our model predictions display a remarkable agreement with experimental data without the need of any tunable parameter. As such, our formulation provides a theoretically sound link between a heterogeneous porous medium structure and its permeability.

POROUS MEDIA STRUCTURE DESIGN

To investigate the link between a heterogeneous porous structure and its intrinsic permeability k , we design 12 two-dimensional porous media whose structure (Ω_i ($i = 1, \dots, 12$)) is composed by N_d non-overlapping, circular and impermeable grains, here represented by N_d circular disks of random position and radius r_j , for $j = 1, \dots, N_d$. Figure 1 shows the 12 porous structures considered in this study. Single phase fluid flow takes place among the circular grains, i.e. the pore space, under the action of an imposed pressure gradient.

We characterize each porous structure by identifying the nearest neighbors of each grain with a Delaunay triangulation associated with the grain centers, as schematically shown in Figure 2 (a,b). Each edge of the triangulation, of length d , connects the centers of two nearest neighboring grains centers of radii r_1 and r_2 . This defines a pore throat of size $\lambda = d - r_1 - r_2$ and each triangle (i.e., a triplet of nearest neighbors) defines a pore body whose center is represented by a red dot in Figure 2(a,b). The size w of a pore body is the length over which the fluid flows while squeezed within a pore throat $w = \ell \sin\theta$, where ℓ is a segment measuring the distance between neighboring pore body centers and θ is the angle between ℓ (red segment in Figure 2 b) and the pore throat λ (blue segment in Figure 2 b).

We note that the media structures are designed to have similar macroscopic quantities: average grain radius \bar{r} , pore throat size $\bar{\lambda}$, pore body size \bar{w} and porosity ϕ , as shown in Figure 2 (c-d-f-e), respectively. These macroscopic values vary at best by a factor of 3, across all porous structures. We further note that grain sizes, pore throats and bodies are also designed to be distributed as broadly as possible. In our scenarios, these span across almost two orders of magnitude, as shown by the sample Probability Density Function (PDF) of r , λ and w shown in Figure 2 (g-h-i), respectively.

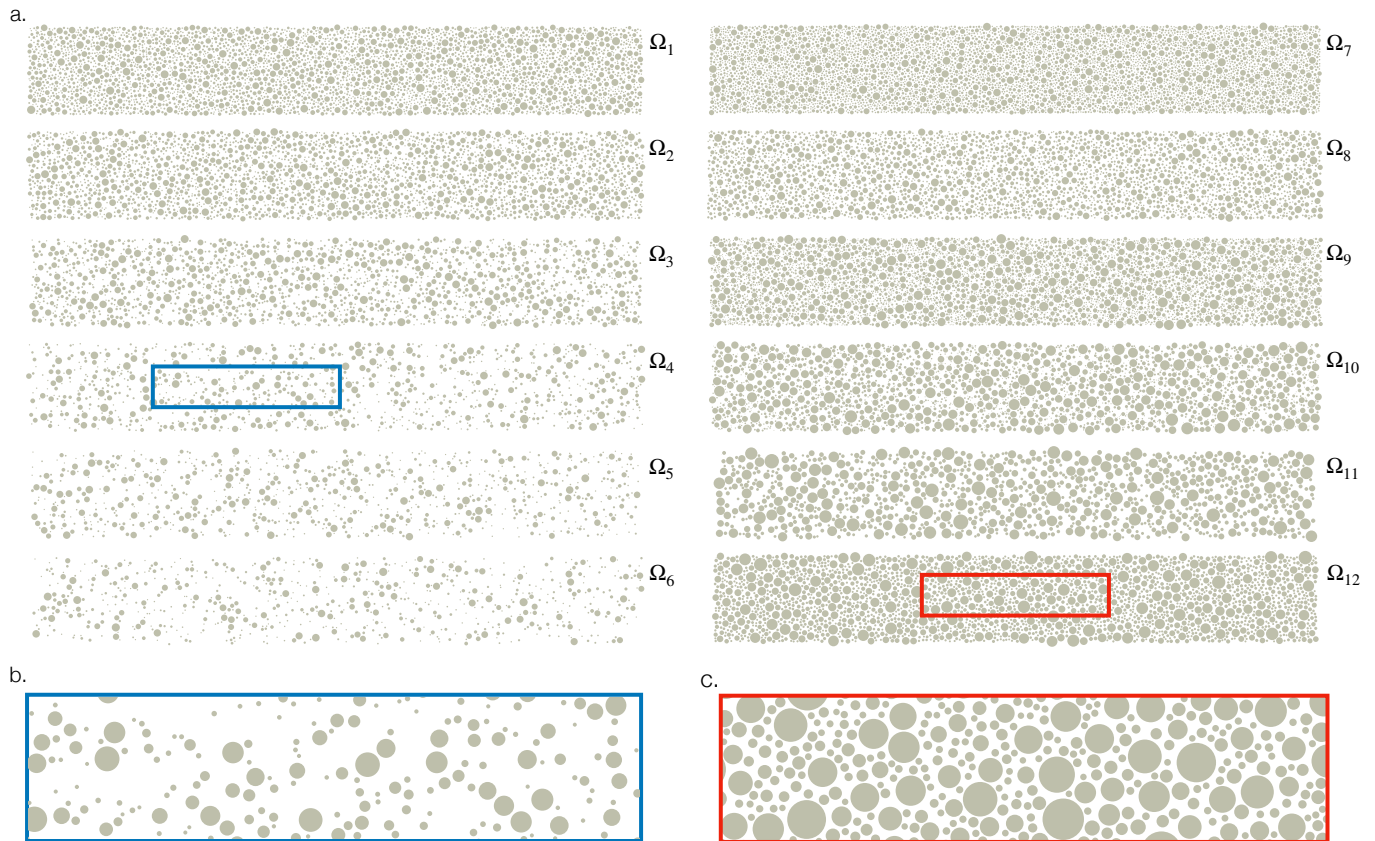


FIG. 1. (a) Representation of the 12 two-dimensional porous geometries Ω_i (Length = 54.5 mm, Width = 3.8 mm) designed in this study, showing the non-overlapping circular disks (gray circles) of random position and radius r_j associated with each geometry. eZoomed-in views of selected regions, i.e., (b) blue corresponding to medium Ω_4 (porosity of 82.6%) and (c) red corresponding to medium Ω_{12} (porosity of 46.0%).

MICROFLUIDICS EXPERIMENTS

We fabricate 12 porous microfluidic devices with the geometries described above and shown in Figure 3 *a*. The solid matrix is composed by cylindrical pillars of vertical thickness $H = 100\mu\text{m}$ (see Figure 3 *c*), each mimicking a grain of the porous medium. The value of H is selected so that it is similar to the average pore throat $\bar{\lambda}$. This avoids plug flow between grains characterized by a flat velocity profile among grains [55, 56]. Fabrication of the microfluidics devices is based on standard soft-lithography [56, 57]. A silicon wafer is spin-coated with the SU-8 2025 permanent epoxy negative photo-resist (*MicroChem*) to pattern a mold based on the designed geometries. Liquid polydimethylsiloxane (PDMS) is prepared as 1:10 by-weight mixture of Curing Agent and Base silicone elastomer (*Sylgard 184, Dow Europe GmbH*). It is, then, poured onto the hard SU-8 mold. All PDMS chips are characterized by the same width $W = 3.8$ mm and length $L = 54.5$ mm. They are pinched for inlet and outlet holes and plasma bonded to a glass slide. To eliminate air bubbles that could be trapped during the water injection, the PDMS is degassed in a desiccator for about 30 minutes before each experiment [55, 58].

The intrinsic permeability k of the system is assessed experimentally by imposing a pressure drop across the porous domain and continuously measuring the corresponding flow rate Q by weighting the outlet reservoir, as described below and shown schematically in Figure 3 *a* and *b*. Inlet and outlet reservoirs are 50 mL falcon tubes closed with gas-tight caps equipped with two threaded ports. One of the ports is connected to a pressure controller (OB11 - MK3, *ElveFlow*) through a tube with an inner diameter of 3 mm. The other port is connected to the microfluidics inlet/outlet with a Tygon tube with inner diameter of 0.5 mm. Pressure in each reservoir is controlled via the pressure controller. The outlet reservoir is placed on an analytical

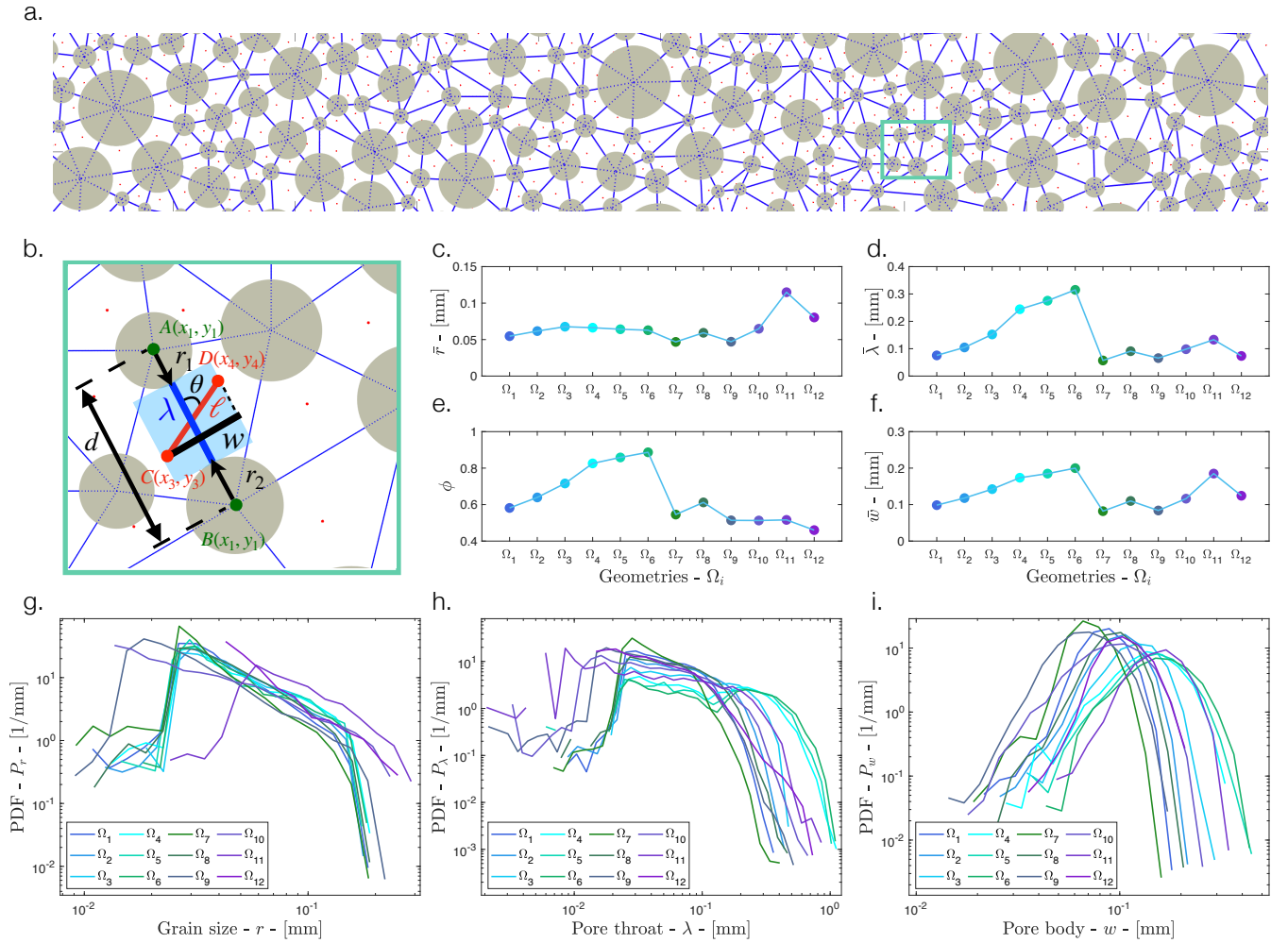


FIG. 2. (a) Details of the Delaunay triangulation of a portion of a pore geometry (edges are marked in blue and their centers with red points). (b) Zoomed-in view of green rectangular in (a). Schematic of the conceptual model of pores as pipes (cyan squares) associated with pore throats λ and pore bodies w . The blue solid line defines a pore throat of size $\lambda = d - r_1 - r_2$; each couple of neighboring triangle of center C and D defines a pore body $w = \ell \sin \theta$, where $\theta = \arccos \frac{AB \cdot CD}{|AB| \cdot |CD|} \in [0, \pi]$. We set that angle to $\pi - \theta$ when it is greater than $\pi/2$. (c) Average grain radius \bar{r} for each geometry Ω_i . (d) Average pore throat $\bar{\lambda}$ for each geometry Ω_i . (e) Porosity ϕ of each geometry Ω_i . (f) Average pore body \bar{w} for each geometry Ω_i . (g) Double logarithmic plot of the probability density function (PDF), P_r , of the grain size r distribution. (h) Double logarithmic plot of the pore throat size λ PDF, P_λ . (i) Double logarithmic plot of the pore body size w PDF, P_w .

scale (XS205DU, *Metzler-Toledo*) that continuously provides measurements of the reservoir weight to a computer, every 0.2 s.

We perform flow experiments for each porous structure by continuously injecting milliQ-water into the previously saturated system. While the outlet pressure P_2 is set to the constant value of 10 mbar, we impose the inlet pressure P_1 to increase linearly with time from 10 mbar to 200 mbar during an interval of 1800 s.

The imposed pressure drops are set to always result in flow rates ensuring laminar flow conditions across the pore space. In other words, our experiments are always characterized by a Reynolds number $Re = \rho \bar{\lambda} q / \mu < 1$, where μ and ρ are the dynamic viscosity and density of water at the experimental temperature conditions (21 C°), respectively. The averaged (Darcy) velocity of the fluid $q = Q/A$ is computed from the measured flow rate Q under the maximum pressure drop $\Delta P_l = P_2 - P_1 = -190 \text{ mbar}$ across the chip cross-sectional area $A = WH$).

The time series t_1 and t_2 at which the inlet/outlet pressures $P_1(t_1)$, $P_2(t_1)$ and the outlet reservoir mass ($M(t_2)$) are measured

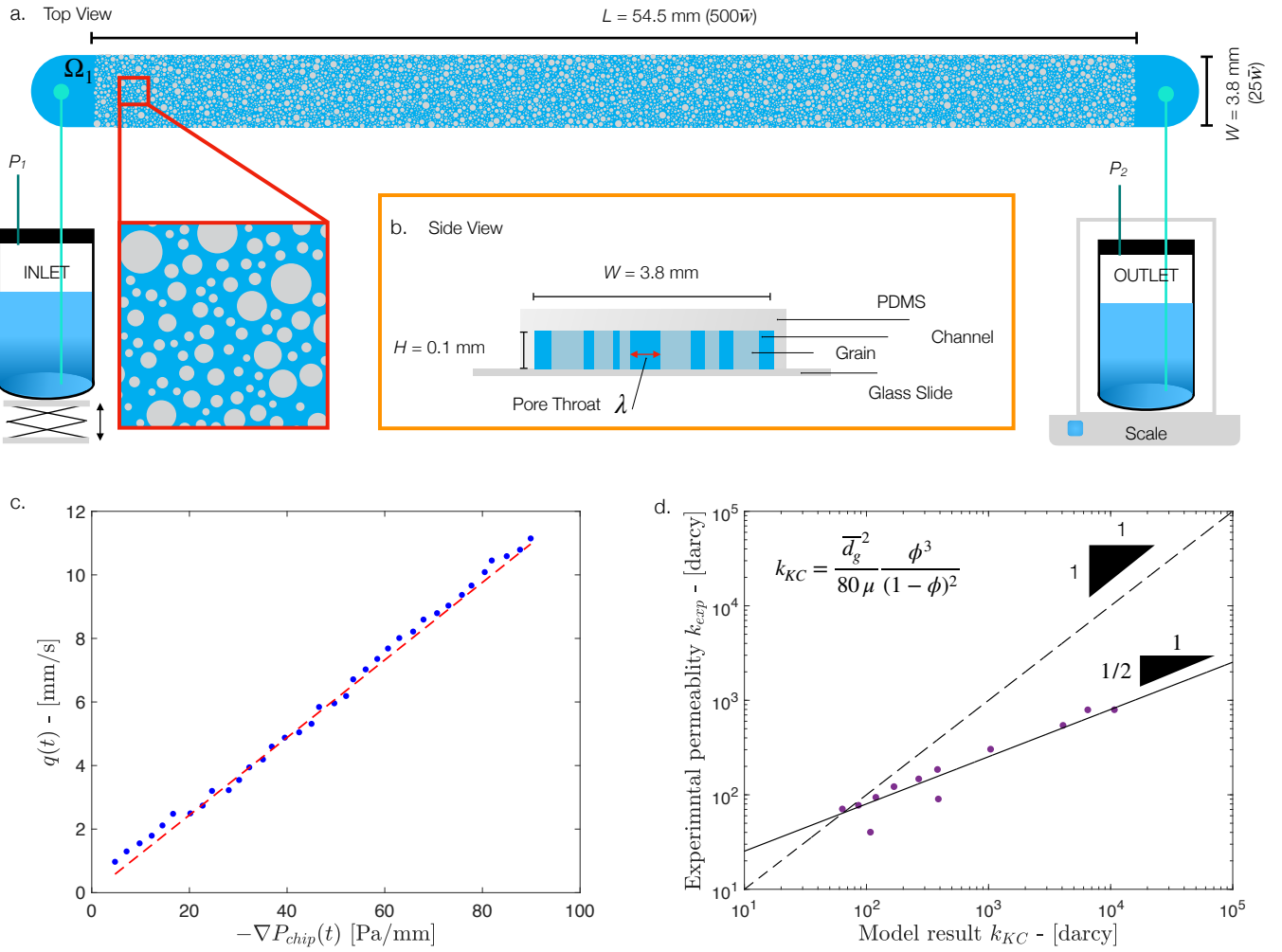


FIG. 3. (a) Schematic view of the experimental set-up to measure the intrinsic permeability of the host medium by imposing a constant pressure gradient across a microfluidic device and continuously weighting the outlet reservoir to measure the associated flow rate. Gray disks correspond to grains, blue background indicates the water that saturates the pore space. The inlet reservoir is positioned on a laboratory jack to regulate water level and guarantee equal head between the two reservoirs and the chip at the beginning of the experiment. The outlet reservoir is placed on an analytical scale to periodically measure its weight. (b) Cross-section of the PDMS microfluidic device with pillars (gray) corresponding to grains, width $W = 3.8$ mm and thickness $H = 0.1$ mm. It is plasma-bonded to a microscopy glass slide, the pore space being shown by the blue patches between the gray pillars. (c) Blue dots represent the Darcy velocity of the porous system under diverse pressure gradient across the chip. The red dashed line represents the best linear fit. (d) Experimental permeability k_{exp} of the 12 heterogeneous media and prediction k_{KC} of the classical Kozeny-Carman formula.

differ as they correspond to data collected by different instruments. Thus, we define a common time t represented by a series of $n = 100$ values from $t_0 = 0$ s and $t_n = 1800$ s, respectively corresponding to the experiment start, i.e. no flow condition $P_{out} = P_{in}$, and its end, when $P_2 = P_1 - 190$ mbar. Thus, the time interval Δt of the common time is $1800/n = 18$ s. We then interpolate linearly pressure and mass data on such common time reference frame. The overall volumetric flow rate at each time, $Q(t)$, is evaluated from the interpolated out-flowing fluid mass, $M(t)$, as $Q(t) = \Delta M(t)/\rho/\Delta t$. Figure 3 (c) depicts Darcy velocity q as a function of the overall (temporally varying) pressure gradient. Finally, we calculate the intrinsic permeability k_{exp} of the microfluidic devices by fitting the Darcy's law

$$q(t) = -\frac{k_{exp}}{\mu} \nabla P_c(t), \quad (3)$$

where $\nabla P_c(t) = \Delta P_c(t)/L_c$ is pressure gradient between the inlet and outlet of the chip. Beside pressure gradient variations that we impose via the pressure controller ($\Delta P_t = P_2 - P_1$), fluid pressure across the chip also varies during the flow experiments due to two mechanisms.

First, we must consider variations in water level within the inlet and outlet reservoirs. The former decreases while the latter increases, as water flows from one reservoir to the other one. Then, pressure losses across the inlet and outlet connecting pipes should also be taken into account. Thus, the pressure drop across the whole device can be expressed as $\Delta P_c(t) = \Delta P_t(t) + \Delta H(t) + \Delta P_l(t)$, where the last two terms represents the mentioned two mechanisms and are defined as follows. Since the inlet-outlet reservoirs have identical cross-sectional area A_r and the water free surface therein is initially located at the same height, the inlet-outlet hydraulic head difference is estimated as twice the water level difference measured within one of the two reservoirs. The latter is equal to twice the volume of water flown since the beginning of the experiment divided by the reservoir cross-sectional area A_r , i.e., $\Delta H(t) = 2(M(t) - M(0))/\rho A_r$. The pressure loss ΔP_l associated with the fluid motion within the connecting pipes is given by the Hagen-Poiseuille law [17] as $\Delta P_l(t) = 8\mu Q(t)L_p/\pi r_p^4$, where L_p and r_p correspond to the length and radius of the Tygon tube, respectively.

The blue dots in Figure 3 (c) represent the experimental data of the measured Darcy velocity $q(t)$ and the pressure gradient $\nabla P_c(t)$ across one of the porous structures designed (Ω_1). Assuming that the data corresponding to Darcy velocity and pressure drop are affected by identically distributed small (about a few percentage) and random errors, we invoke the maximum likelihood principle to analytically calculate the best fit and estimate for the linear relationship coefficient, from the series of n measured values of q and ∇P_c [59]. Thus, we evaluate the intrinsic medium permeability k_{exp} from the linear fit of eq. (3) as:

$$k_{exp} = \frac{n \sum_{i=1}^n ((-\nabla P_{ci}/\mu) q_i) - \sum_{i=1}^n (-\nabla P_{ci}/\mu) \sum_{i=1}^n (q_i)}{n \sum_{i=1}^n (-\nabla P_{ci}/\mu)^2 - (\sum_{i=1}^n (-\nabla P_{ci}/\mu))^2}, \quad (4)$$

where its uncertainty is given by [59],

$$\delta_{k_{exp}} = \delta_q \sqrt{\frac{n}{n \sum_{i=1}^n (-\nabla P_{ci}/\mu)^2 - (\sum_{i=1}^n (-\nabla P_{ci}/\mu))^2}} \quad (5)$$

and

$$\delta_q = \sqrt{\frac{1}{n-2} \sum_{i=1}^n (q_i - \frac{n \sum_{i=1}^n ((-\nabla P_{ci}/\mu)^2 \sum_{i=1}^n q_i) - \sum_{i=1}^n (-\nabla P_{ci}/\mu) \sum_{i=1}^n ((-\nabla P_{ci}/\mu) q_i)}{\sum_{i=1}^n (-\nabla P_{ci}/\mu)^2 - (\sum_{i=1}^n (-\nabla P_{ci}/\mu))^2} - k_{exp} (-\nabla P_{ci}/\mu))^2}. \quad (6)$$

The resulting permeability values are listed in Table I. These vary within the range [40.2, 794] darcy (i.e., spanning more than one order of magnitude) with relative uncertainty $\delta_{k_{exp}}/k_{exp}$ ranging between 0.2% and 8% (average value over the set of 12 structures being 2%).

Structure	Ω_1	Ω_2	Ω_3	Ω_4	Ω_5	Ω_6	Ω_7	Ω_8	Ω_9	Ω_{10}	Ω_{11}	Ω_{12}
porosity ϕ [-]	58.1%	63.9%	71.6%	82.6%	85.8%	88.7%	54.5%	61.2%	51.4%	51.3%	51.6%	46.0%
permeability k_{exp} [darcy]	122	185	303	542	792	794	77.4	147.2	71	94.1	90.2	40.2
uncertainty $\delta_{k_{exp}}$ [darcy]	1.5	3	8	16	40	68	0.5	2	0.2	0.6	0.7	0.2

TABLE I. Values of intrinsic permeability k_{exp} and its related uncertainty $\delta_{k_{exp}}$ obtained for the 12 designed porous systems via linear interpolation of collected data [59]. The relative uncertainty $\delta_{k_{exp}}/k_{exp}$ results to range within the interval [0.2%-8%] with averaged value over the set of 12 structures being 2%.

Figure 3 (d) shows the experimentally based values of the 12 porous media permeability listed in table I against the classical Kozeny-Carman prediction, eq. (2). As stated above, the latter provides an estimate of the medium permeability upon considering the resistance to flow as rendered by the Hagen Poiseuille law, accounting for the actual friction experienced by the fluid through an equivalent medium composed of identical grains of size d_g equal to the average grain size (gray disks in Figure 1). For an assemblage of cylinders, $c_0/\sigma = d_g^2/80$, which yields

$$k_{KC} = \frac{d_g^2}{80\mu} \frac{\phi^3}{(1-\phi)^2}, \quad (7)$$

where $d_g = \bar{r}$ is a mean grain diameter and ϕ is the medium porosity.

This result does not provide an appropriate representation of the experimental data, both in terms of actual values and scaling pattern. The key reason for this discrepancy is that the Kozeny-Carman formulation does not explicitly takes into account the variability of the porous structures. In other words, the average grain size and porosity values are not representative of the structural variability of the medium, that should be taken into account.

PORE SIZE VARIABILITY CONTROL ON POROUS MEDIUM PERMEABILITY

To take into account the impact of the spatial variability of the pore space across the medium structure and upscale it to a consistent and sound assessment of the medium permeability, we consider the whole system as a collection of m virtual porous systems in series. Each of these is characterized by a length l_i ($i = 1, \dots, m$) along the mean flow direction and a permeability k_i . The number of porous media of average length \bar{l} needed to cover the system size is $m = L/\bar{l}$. In the following, we directly relate permeability k_i and length l_i to the actual medium structural properties.

We start by considering the overall pressure drop ΔP_p experienced by a fluid particle p flowing with average velocity q along its trajectory of length $L' = L\tau$, where $\tau = L'/L$ represents the medium tortuosity, (as schematically shown in Figure 4 (a)). As the

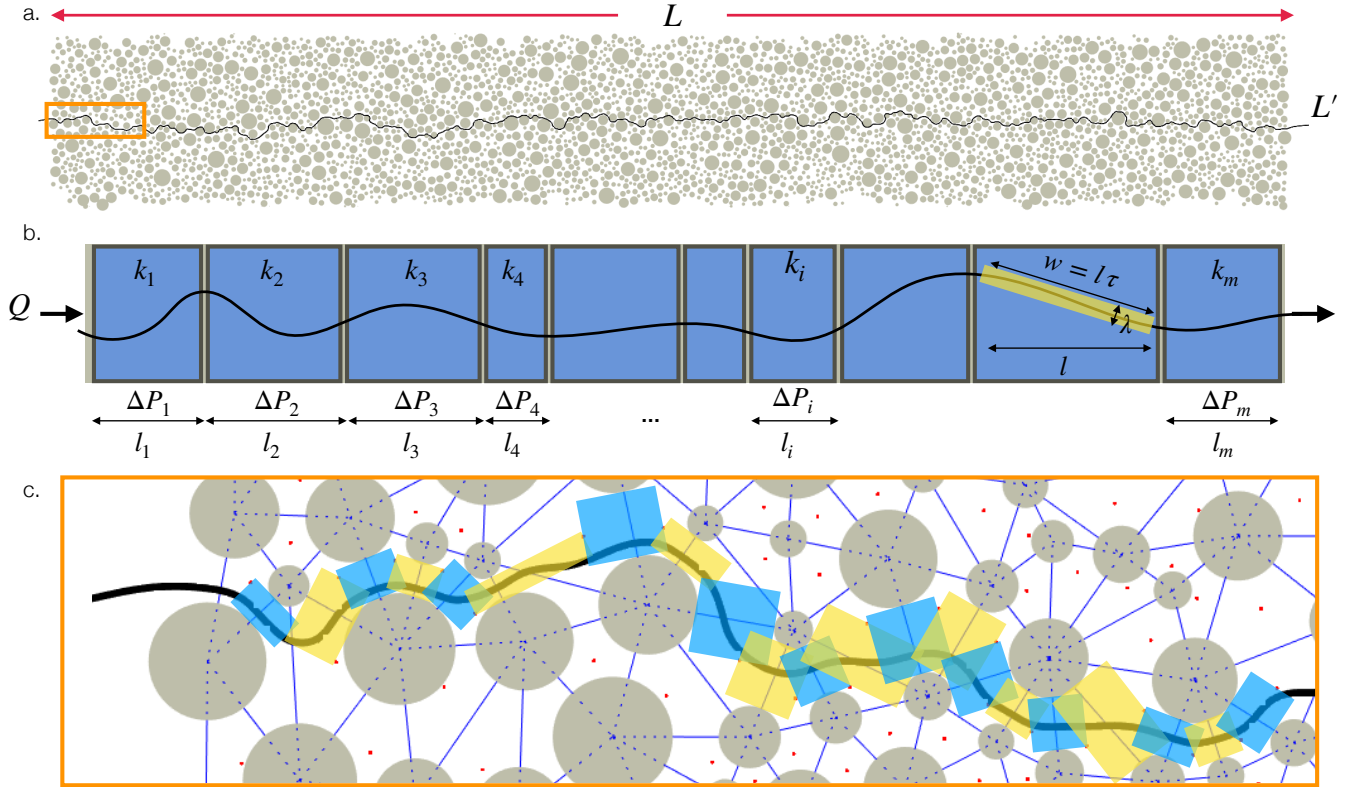


FIG. 4. (a) Two-dimensional (2D) representation of the porous geometry Ω_1 with a trajectory generated from particle tracking simulations through the numerically computed velocity field across the system. (b) Schematic view of our model, conceptualizing the system as a series of porous media of individual length l_i and permeability k_i . (c) Zoomed-in view of the orange rectangle in (a); the trajectory moves across pores as they were pipes of diameter equal to the local pore throat and length equal to the local pore body.

fluid particle moves across the series of m smaller porous media, the pressure drop ΔP can be viewed as the sum of all pressure drops ΔP_i across each of individual medium of length l_i (as in Figure 4 (b)), i.e.,

$$\Delta P = -\frac{q\mu L\tau}{k} = -\sum_{i=1}^m q\mu \frac{l_i}{k_i}. \quad (8)$$

The overall permeability k is, then, estimated as the following harmonic average

$$k = \frac{L\tau}{\sum_{i=1}^m \frac{l_i}{k_i}}. \quad (9)$$

To relate the permeability k_i and length l_i of each of the m porous media described above to the pore scale structural properties of the actual medium, we consider that the smallest portion of the macroscopic system that can host fluid flow is the individual pore. Thus, we assume that the value of permeability k_i is the one of a pipe with diameter equal to a pore throat λ , i.e., $k_i = \lambda_i^2/32$ (as

in Figure 4 (c)). The length l_i of such a flow system equals the length of a pore body divided by the system tortuosity $l_i = w_i/\tau$, thus enabling one to take into account the random orientation of the local fluid flow direction with respect to the average flow (see Figure 4 (b,c)). From a macroscopic perspective, the porous medium is, thus, conceptualized as composed by a series of $m = L\tau/\bar{w}$ individual porous systems, with overall permeability k_t that depends on the microscopic pore throat λ and body w sizes according to

$$k_t = \frac{L\tau}{\sum_{i=1}^m \frac{l_i}{k_i}} = \frac{L\tau^2}{\sum_{i=1}^m \frac{32w_i}{\lambda_i^2}}. \quad (10)$$

Figure 6 (a) shows as green dots the scatter-plot of our measured permeability k_{exp} and our model results (eq. (10)). It also includes the corresponding prediction based on the Kozeny-Carman formula (pink dots). We quantify the accuracy of our results across all designed 12 porous geometries in terms of the mean squared discrepancy χ between experimentally measured data k_{exp} and model results k_t :

$$\chi = \sqrt{\frac{1}{N} \sum_{s=1}^N \left(\frac{k_{ts} - k_{exp_s}}{k_{exp_s}} \right)^2}. \quad (11)$$

While $\chi = 32\%$ for our model, the Kozeny-Carman prediction yields a value of $\chi = 476\%$.

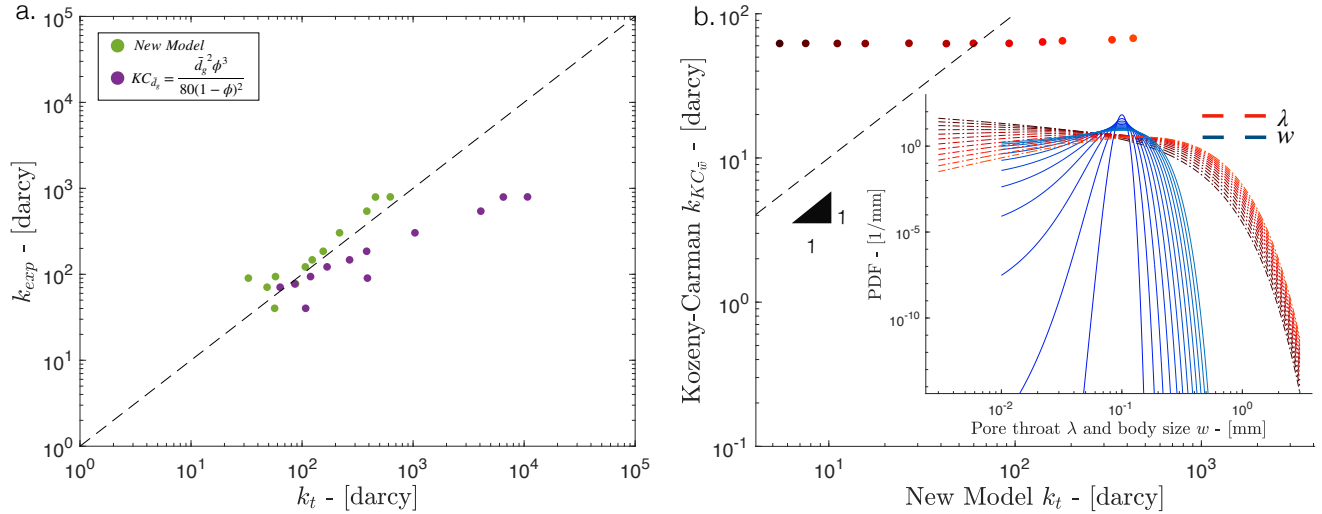


FIG. 5. (a) Scatter-plot of experimental permeability measured for the heterogeneous media designed versus the prediction of (i) our model eq. (10) (green dots) or (ii) the Kozeny-Carman formula using the average grain diameter (pink dots) or average pore throat (pink stars) as characteristic length scale; (b) Scatter-plot of permeability values obtained through our model vs those obtained through the Kozeny-Carman formulation for 12 additional pore size broader distributions (shown in inset) characterized by the same averaged value.

To test the robustness of our findings, we repeat the analysis upon defining pore sizes across the porous domains through a MIC (Maximum Inscribed Circles) algorithm [56, 60, 61] (see Figure 6 (a,b)). This approach relies on centering a circle that touches the closest grain at each point of the pore space skeleton (see red disks in Figure 6). We, then, consider each circle defined by the MIC algorithm to represent the individual pores, where the throat λ_{mic} and body w_{mic} sizes are both equal to the circle diameter d_{MIC} . Embedding this approach in our formulation yields a value of $\chi = 35\%$, similar to the prediction obtained with the triangulation method, highlighting the robustness of our model.

We note that to ensure a parabolic fluid velocity profile between grains and avoid plug flow the microfluidics structures are limited by their own thickness. Thus, as discussed above, the ratio between largest and smallest size of throats or bodies is limited to around 80 (see Figure 2 (h,i)). To further strengthen the relevance of our model, we then generate 12 additional virtual pore throat and body size distributions that are broader than what we could fabricate. These synthetic pore space distributions have all by the same porosity $\phi = 0.5$, average pore throat $\bar{\lambda} = 0.09$ mm and pore body size $\bar{w} = 0.1$ mm. The corresponding distributions (as rendered through sample PDFs) of w (blue dashed curves) and λ (red dashed curves) are shown in the inset of Figure 6 (b), where we depict a scatter plot of permeability values obtained through our model (eq. (10)) versus those obtained

through the Kozeny-Carman formula (eq. (7)). While the latter predicts the same permeability for all the 12 geometries, since they have been designed to have the same macroscopic properties, our model taking into account the detailed pore size variability returns very different values.

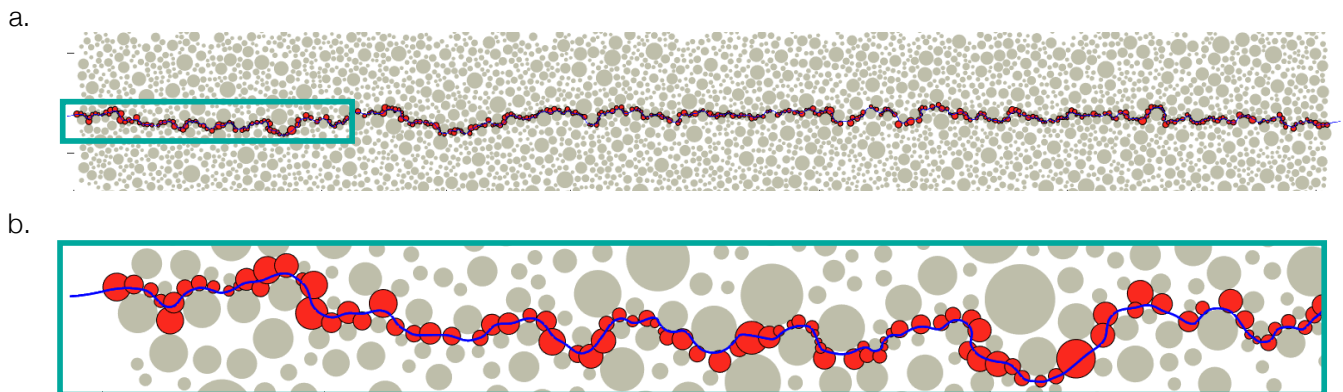


FIG. 6. (a) The 2D porous geometry Ω_1 with an exemplary trajectory (blue curve) generated from particle tracking based on a numerical solution of the velocity field. (b) Zoomed-in view of the green rectangle in (a); solid red circles (MICs) represents pores along the trajectory.

CONCLUSION

Despite the relevance of flow through porous media and related (flow-driven) processes, the dependence of a heterogeneous medium intrinsic permeability from its structural properties is still not fully understood. Here, we investigate this long-standing challenge by designing a set of heterogeneous porous structures that differ in the statistical distribution of their pore size. The latter span across more than one order of magnitude in our systems. We quantify their permeability with a novel experimental method by flowing water through microfluidics replicating a set of designed and complex porous structures, by imposing a controlled pressure gradient and continuously measuring the resulting fluid flow rate.

The classical Kozeny-Carman formulation fails at rendering the permeability of all of the 12 structures analyzed, both in terms of values and scaling features. We then propose a new model that fully takes into account the structural variability of pore sizes and predicts the experimentally-based intrinsic permeability without the need of any fitting/tunable parameter.

We incorporate the structural heterogeneity of the porous media analyzed by conceptualizing their macroscopic structure as composed by m smaller porous media placed in series. We relate their number, m , individual length and permeability to the structural medium properties via the Hagen-Poiseuille law, describing flow through a pipe. We show that knowledge of the pore size λ distribution is enough to accurately assess the overall intrinsic permeability for the scenarios that we analyzed. Our model fully embeds the system tortuosity and establishes the hydraulic equivalence between the overall porous medium and a system of m porous media in series with the same hydraulic properties of pipes with diameter λ . Hence, the medium permeability corresponds to the harmonic mean of m individual permeability values $\lambda_i^2/32$ ($i = 1, \dots, m$) each weighted by the body size.

ACKNOWLEDGEMENTS

PdA acknowledges the support from the FET-Open project NARCISO (ID: 828890) and of Swiss National Science Foundation (grant ID 200021_219863). WJ acknowledges the funding of China Scholarship Council for financial support through the fellowship (grant ID: CSC202008210309). AG acknowledges support from the European Union Next-Generation EU (National Recovery and Resilience Plan - NRRP, Mission 4, Component 2, Investment 1.3 - D.D. 1243 2/8/2022, PE0000005) in the context of the RETURN Extended Partnership. All authors thank Monica Riva, Martina Siena and Chiara Recalcati for useful and insightful discussions.

* Corresponding author: pietro.deanna@unil.ch

- [1] Stefan Banzhaf, Andreas Krein, and Traugott Scheytt. Investigative approaches to determine exchange processes in the hyporheic zone of a low permeability riverbank. *Hydrogeology Journal*, 19(3):591–601, 2011.
- [2] Sha Qiu, Wenqing Cao, Zhiguo Chen, Yiyun Liu, Jingpeng Song, Rong Zhang, and He Bai. Experiments and mechanisms for leaching remediation of lead-contaminated soil by enhancing permeability. *Chemical Engineering Journal*, page 130720, 2021.
- [3] Noriaki Watanabe, Kohei Saito, Atsushi Okamoto, Kengo Nakamura, Takuya Ishibashi, Hanae Saishu, Takeshi Komai, and Noriyoshi Tsuchiya. Stabilizing and enhancing permeability for sustainable and profitable energy extraction from superhot geothermal environments. *Applied Energy*, 260:114306, 2020.
- [4] Silvio B Giger, Eric Tenthorey, Stephen F Cox, and John D Fitz Gerald. Permeability evolution in quartz fault gouges under hydrothermal conditions. *Journal of Geophysical Research: Solid Earth*, 112(B7), 2007.
- [5] Marco De Paoli, Francesco Zonta, and Alfredo Soldati. Influence of anisotropic permeability on convection in porous media: Implications for geological CO₂ sequestration. *Physics of fluids*, 28(5):056601, 2016.
- [6] Krzysztof M Graczyk and Maciej Matyka. Predicting porosity, permeability, and tortuosity of porous media from images by deep learning. *Scientific Reports*, 10(1):1–11, 2020.
- [7] Liang Luo, Boming Yu, Jianchao Cai, and Xiangfeng Zeng. Numerical simulation of tortuosity for fluid flow in two-dimensional pore fractal models of porous media. *Fractals*, 22(04):1450015, 2014.
- [8] YF Liu and DS Jeng. Pore scale study of the influence of particle geometry on soil permeability. *Advances in Water Resources*, 129:232–249, 2019.
- [9] James M Sperry and J Jeffrey Peirce. A model for estimating the hydraulic conductivity of granular material based on grain shape, grain size, and porosity. *Groundwater*, 33(6):892–898, 1995.
- [10] Allison Cormican, JF Devlin, and Craig Divine. Grain size analysis and permeability for estimating hydraulic conductivity in engineered porous media. *Groundwater Monitoring & Remediation*, 40(2):65–72, 2020.
- [11] Qinjun Kang, Li Chen, Albert J Valocchi, and Hari S Viswanathan. Pore-scale study of dissolution-induced changes in permeability and porosity of porous media. *Journal of Hydrology*, 517:1049–1055, 2014.
- [12] Henry Darcy. *Les fontaines publiques de la ville de Dijon: exposition et application...* Victor Dalmont, 1856.
- [13] Jacob Bear. *Dynamics of fluids in porous media*. Courier Corporation, 1988.
- [14] JE Drummond and MI0598 Tahir. Laminar viscous flow through regular arrays of parallel solid cylinders. *International Journal of Multiphase Flow*, 10(5):515–540, 1984.
- [15] Arndt Wagner, Elissa Eggenweiler, Felix Weinhardt, Zubin Trivedi, David Krach, Christoph Lohrmann, Kartik Jain, Nikolaos Karadimitriou, Carina Bringedal, Paul Voland, et al. Permeability estimation of regular porous structures: A benchmark for comparison of methods. *Transport in Porous Media*, 138(1):1–23, 2021.
- [16] A Koponen, M Kataja, and J Timonen. Permeability and effective porosity of porous media. *Physical Review E*, 56(3):3319, 1997.
- [17] SP Suter and R Shalak. The history of poiseuille’s law. *annual review of fluid mechanics*. 25: 1, 19, 1993.
- [18] RR Sullivan and KL Hertel. The permeability method for determining specific surface of fibers and powders. *Advances in colloid science*, 1:37–80, 1942.
- [19] Xiaohu Yang, Tian Jian Lu, and Tongbeum Kim. An analytical model for permeability of isotropic porous media. *Physics Letters A*, 378(30-31):2308–2311, 2014.
- [20] Naoki Nishiyama and Tadashi Yokoyama. Permeability of porous media: Role of the critical pore size. *Journal of Geophysical Research: Solid Earth*, 122(9):6955–6971, 2017.
- [21] Raphael Schulz, Nadja Ray, Simon Zech, Andreas Rupp, and Peter Knabner. Beyond kozeny–carman: predicting the permeability in porous media. *Transport in Porous Media*, 130(2):487–512, 2019.
- [22] Shun Nomura, Yuzuru Yamamoto, and Hide Sakaguchi. Modified expression of kozeny–carman equation based on semilog–sigmoid function. *Soils and Foundations*, 58(6):1350–1357, 2018.
- [23] Dvorkin Jack. Kozeny-carman equation revisited. 2009.
- [24] Johannes Hommel, Edward Coltman, and Holger Class. Porosity–permeability relations for evolving pore space: a review with a focus on (bio-) geochemically altered porous media. *Transport in Porous Media*, 124(2):589–629, 2018.
- [25] J Kozeny. Über kapillare leitung des wassers im boden: Sitzungsberichte der wiener akademie der wissenschaften. 1927.
- [26] PC Carman. Fluid flow through a granular bed: Transactions of the institution of chemical engineers, 1937.
- [27] L Skartsis, JL Kardos, and B Khomami. Resin flow through fiber beds during composite manufacturing processes. part i: Review of newtonian flow through fiber beds. *Polymer Engineering & Science*, 32(4):221–230, 1992.
- [28] M. J. Blunt et al. Pore-scale imaging and modelling. *Adv. Water Resour.*, 51:97–216, 2013.
- [29] I. Gueven, S. Frijters, H. Harting, S. Luding, and H. Steeb. Hydraulic properties of porous sintered glass bead systems. *Granular Matter*, page 19:28, 2017.
- [30] Kazutaka Mizutani, Hideki Minagawa, Kotaro Ohga, Naoya Takahara, Yasuhide Sakamoto, Takeshi Komai, Tsutomu Yamaguchi, and Hideo Narita. Relation between pore size distribution and permeability of sediment consist of glass beads and sand. *Journal of the Japanese Association for Petroleum Technology*, 75(2):164–176, 2010.
- [31] Desbois G. Hemes, S., J. L. Urai, B. Schroppel, and J. O. Schwarz. Multi-scale characterization of porosity in boom clay (hades-level, mol, belgium) using a combination of x-ray μ -ct, 2d bib-sem and fib-sem tomography. *Microporous Mesoporous Mater.*, 2018:1–20, 2015.
- [32] J. Zhao, Z. Jin, Q. Hu, Z. Jin, T. J. Barber, Y. Zhang, and M. Bleuel. Integrating sans and fluid invasion methods to characterize pore structure of typical american shale oil reservoirs. *Sci. Rep.*, 7:15413, 2017.

- [33] Ngoc-Son Nguyen, Habib Taha, and Didier Marot. A new delaunay triangulation-based approach to characterize the pore network in granular materials. *Acta Geotechnica*, 16(7):2111–2129, 2021.
- [34] Jeff T Gostick. Random pore network modeling of fibrous pemfc gas diffusion media using voronoi and delaunay tessellations. *Journal of the Electrochemical Society*, 160(8):F731, 2013.
- [35] Shengyan Gao, Jay N Meegoda, and Liming Hu. Two methods for pore network of porous media. *International Journal for Numerical and Analytical Methods in Geomechanics*, 36(18):1954–1970, 2012.
- [36] Songlin Liu, Liang Wang, Yongdong Jiang, Wenqian Wang, Minggao Yu, Haitao Li, Mingqiu Wu, and Wenjie Xu. Random pore-network development methodology based on voronoi and delaunay tessellations for residual coal under axial stress. *Fuel*, 353:129267, 2023.
- [37] Bagus P Muljadi, Martin J Blunt, Ali Q Raeini, and Branko Bijeljic. The impact of porous media heterogeneity on non-darcy flow behaviour from pore-scale simulation. *Advances in water resources*, 95:329–340, 2016.
- [38] P. de Anna, B. Quafe, G. Birois, and R. Juanes. Prediction of low velocity distribution from the pore structure in simple porous media. *Phys. Rev. Fluids*, 124103, 2017.
- [39] Karen Alim, Shima Parsa, David A Weitz, and Michael P Brenner. Local pore size correlations determine flow distributions in porous media. *Physical review letters*, 119(14):144501, 2017.
- [40] Peng Xu and Boming Yu. Developing a new form of permeability and kozeny–carman constant for homogeneous porous media by means of fractal geometry. *Advances in water resources*, 31(1):74–81, 2008.
- [41] Jeffrey D Hyman, Piotr K Smolarkiewicz, and C Larrabee Winter. Pedotransfer functions for permeability: a computational study at pore scales. *Water Resources Research*, 49(4):2080–2092, 2013.
- [42] Amir Raoof and S Majid Hassanizadeh. A new method for generating pore-network models of porous media. *Transport in porous media*, 81:391–407, 2010.
- [43] Yang Liu, Wenbo Gong, Yu Zhao, Xu Jin, and Moran Wang. A pore-throat segmentation method based on local hydraulic resistance equivalence for pore-network modeling. *Water Resources Research*, 58(12):e2022WR033142, 2022.
- [44] Qingrong Xiong, Todor G Baychev, and Andrey P Jivkov. Review of pore network modelling of porous media: Experimental characterisations, network constructions and applications to reactive transport. *Journal of contaminant hydrology*, 192:101–117, 2016.
- [45] Andrey P Jivkov, Cathy Hollis, Friday Etese, Samuel A McDonald, and Philip J Withers. A novel architecture for pore network modelling with applications to permeability of porous media. *Journal of hydrology*, 486:246–258, 2013.
- [46] Choah Shin, Azhar Alhammali, Lisa Bigler, Naren Vohra, and Małgorzata Peszynska. Coupled flow and biomass-nutrient growth at pore-scale with permeable biofilm, adaptive singularity and multiple species. *Mathematical Biosciences and Engineering*, 18(3):2097–2149, 2021.
- [47] Lauren E Beckingham. Evaluation of macroscopic porosity-permeability relationships in heterogeneous mineral dissolution and precipitation scenarios. *Water Resources Research*, 53(12):10217–10230, 2017.
- [48] Reydick D Balucan, Luc G Turner, and Karen M Steel. Acid-induced mineral alteration and its influence on the permeability and compressibility of coal. *Journal of Natural Gas Science and Engineering*, 33:973–987, 2016.
- [49] Bowen Ling, Mo Sodwatana, Arjun Kohli, Cynthia M Ross, Adam Jew, Anthony R Kovscek, and Ilenia Battiato. Probing multiscale dissolution dynamics in natural rocks through microfluidics and compositional analysis. *Proceedings of the National Academy of Sciences*, 119(32):e2122520119, 2022.
- [50] Chuangzhou Wu, Jian Chu, Shifan Wu, and Yi Hong. 3d characterization of microbially induced carbonate precipitation in rock fracture and the resulted permeability reduction. *Engineering Geology*, 249:23–30, 2019.
- [51] Mark O Cuthbert, Lindsay A McMillan, Stephanie Handley-Sidhu, Michael S Riley, Dominique J Tobler, and Vernon R Phoenix. A field and modeling study of fractured rock permeability reduction using microbially induced calcite precipitation. *Environmental science & technology*, 47(23):13637–13643, 2013.
- [52] Yves Bernabé, M Zamora, Min Li, A Maineult, and Yan-Bing Tang. Pore connectivity, permeability, and electrical formation factor: A new model and comparison to experimental data. *Journal of Geophysical Research: Solid Earth*, 116(B11), 2011.
- [53] Davud Davudov and Rouzbeh Ghanbarnezhad Moghanloo. Impact of pore compressibility and connectivity loss on shale permeability. *International Journal of Coal Geology*, 187:98–113, 2018.
- [54] Davud Davudov, Rouzbeh Ghanbarnezhad Moghanloo, and Yixin Zhang. Interplay between pore connectivity and permeability in shale sample. *International Journal of Coal Geology*, 220:103427, 2020.
- [55] Pietro de Anna, Amir A Pahlavan, Yutaka Yawata, Roman Stocker, and Ruben Juanes. Chemotaxis under flow disorder shapes microbial dispersion in porous media. *Nature Physics*, 17(1):68–73, 2021.
- [56] Ankur Deep Bordoloi, David Scheidweiler, Marco Dentz, Mohammed Bouabdellaoui, Marco Abbarchi, and Pietro de Anna. Structure induced laminar vortices control anomalous dispersion in porous media. *Nature communications*, 13(1):3820, 2022.
- [57] Younan Xia and George M Whitesides. Soft lithography. *Angewandte Chemie International Edition*, 37(5):550–575, 1998.
- [58] David Scheidweiler, Ankur Deep Bordoloi, Wenqiao Jiao, Vladimir Sentchilo, Monica Bollani, Audam Chhun, Philipp Engel, and Pietro de Anna. Spatial structure, chemotaxis and quorum sensing shape bacterial biomass accumulation in complex porous media. *Nature Communications*, 15(1):191, 2024.
- [59] John Robert Taylor and William Thompson. *An introduction to error analysis: the study of uncertainties in physical measurements*, volume 2. Springer, 1982.
- [60] Dmitriy Silin and Tad Patzek. Pore space morphology analysis using maximal inscribed spheres. *Physica A: Statistical mechanics and its applications*, 371(2):336–360, 2006.
- [61] Kirill M Gerke, Timofey O Sizonenko, Marina V Karsanina, Efim V Lavrukhin, Vladimir V Abashkin, and Dmitry V Korost. Improving watershed-based pore-network extraction method using maximum inscribed ball pore-body positioning. *Advances in water resources*, 140:103576, 2020.